




Cite this: *Nanoscale Adv.*, 2019, 1, 2748

Enhanced photocatalysis and bacterial inhibition in Nb₂O₅ via versatile doping with metals (Sr, Y, Zr, and Ag): a critical assessment†

Bhanupriya Boruah,  Rimzhim Gupta, Jayant M. Modak and Giridhar Madras *

Unique optical properties render semiconductor Nb₂O₅ nanoparticles suitable for light harvesting and photocatalytic applications. This study focuses on determining optical properties such as the band gap, conduction band edge, valence band edge and work function of as-prepared solution combustion synthesized Nb₂O₅ nanoparticles with the help of UV-vis Diffuse Reflectance spectroscopy (DRS) and ultraviolet photoelectron spectroscopy (UPS) techniques. Phase purity and the oxidation states of the elements present in the material were confirmed from X-ray diffraction (XRD) patterns and X-ray photoelectron spectra (XPS), respectively. Doping semiconductors with different metal ions impacts the activity of the material, and therefore efforts were made to understand the effect on the photocatalytic performance of Nb₂O₅ due to the incorporation of metal dopants viz. Sr, Y, Zr, and Ag. Lattice parameters were obtained from Rietveld refinement of the XRD patterns. Parameters which are closely related to the photoactivity of the catalysts such as the presence of surface defects, oxygen vacancies, surface area, and charge carrier dynamics were determined from photoluminescence (PL) analysis, Brunauer–Emmett–Teller (BET) surface area measurements and time-resolved fluorescence (TRF) analysis respectively. In addition, the dopant concentrations were optimised for enhanced photocatalytic activity. The doped Nb₂O₅ nanoparticles showed significant activity towards targeted degradation of organic pollutants like 2-chlorophenol (2-CP) and dye contaminants like methylene blue (MB), orange G (OG) and indigo carmine (IC). This strategy yielded a robust response towards inactivation of *E. coli* and *S. aureus* as well. Adsorption and photodegradation of MB followed Lagergren's pseudo 1st order reaction model and the Langmuir Hinshelwood model respectively. Bacterial inactivation and OG, IC and 2-CP photodegradation followed 1st order kinetics. The reusability of the catalyst for 5 cycles was demonstrated. Finally, a plausible mechanism is proposed based on radical trapping experiments and combined analysis of the characterization techniques.

Received 16th May 2019

Accepted 30th May 2019

DOI: 10.1039/c9na00305c

rsc.li/nanoscale-advances

1 Introduction

Water pollution from industrial discharges is a major global concern and tackling such problems requires effective environment-friendly water treatment technology.¹ Dyes are a kind of pollutants produced from textile, paint, paper, food, and leather industries. About 280 000 tons of dyes are discharged every year into the aquatic system.² Chlorophenols representing another class of water pollutants, which are considered toxic to humans by the US EPA, are mainly produced from petroleum and pesticide manufacturing industries.³ Apart from these pollutants, water contaminated from coliform bacteria also poses serious health threats.^{4,5} To address these

issues, conventional water treatment methods such as adsorption,⁶ coagulation,⁷ filtration,⁸ and ion exchange⁹ are found to be effective but they lead to the generation of secondary pollutants. Traditional disinfection methods such as using UV light are costly^{10,11} and chlorination generates harmful by-products.^{12,13} Advanced oxidation processes (AOPs) have been used as an alternative for wastewater treatment since the 1990s. Among AOPs, heterogeneous photocatalysis has shown great potential in disinfecting water and degrading chemical contaminants.¹⁴

Photocatalysis involves the usage of semiconductors that function as a catalyst on exposure to irradiation. The photo-generated charge carriers from the semiconductor produce reactive oxygen species to carry out the photodegradation of pollutants.¹⁵ TiO₂ and ZnO are regarded as efficient photocatalysts for water decontamination^{16,17} and have a band gap of around 3–3.2 eV.^{18–20} A similar band gap is observed in Nb₂O₅ which is an n-type semiconductor.²¹ It is broadly utilized in the fields of gas sensing,²² glass manufacturing,²³ and

Department of Chemical Engineering, Indian Institute of Science, Bangalore 560012, India. E-mail: giridhar@chemeng.iisc.ernet.in; Fax: +91 80 23600683; Tel: +91 80 22932321

† Electronic supplementary information (ESI) available. See DOI: 10.1039/c9na00305c



electrochemical energy storage,²⁴ but limited reports are available on Nb₂O₅ as a photocatalyst and its related photochemical properties.^{21,25,26} As Nb₂O₅ exhibits similar semiconducting properties to those of TiO₂, this material has great potential to replace the widely studied titania.

The efficiency of photocatalyzed reactions can reduce due to charge carrier recombination. This can be avoided by doping semiconductors with metal or non-metal impurities.²⁷ Dopants should serve as the trapping sites for electrons or holes to increase the activity of photocatalysts.²⁸ Doping leads to the creation of local energy states in the forbidden gap and could also narrow the band gap.²⁹ Additionally, dopant incorporation could change the particle size, specific surface area, and morphology of nanoparticles which impacts the photoactivity.³⁰ Sood *et al.* found that Sr²⁺ doping enhanced the photocatalytic activity of TiO₂ towards brilliant green degradation due to an increase in the surface area and delay in the recombination time of excitons.³¹ Similar changes in the properties of TiO₂ due to the incorporation of the Y³⁺ dopant were observed and the doped material showed excellent activity towards MO photodegradation.³² Silver doping in TiO₂ was found to red shift the absorption range and enhance the separation efficiency of electrons and holes, thus showing good photocatalytic activity in the visible region towards Cr(VI) reduction.³³ Incorporation of Zr⁴⁺ into TiO₂ resulted in lattice defects and showed higher photoactivity towards the degradation of rhodamine B.³⁴ Extensive studies were performed on doped TiO₂ systems but the literature contains few efforts on the photoelectrochemical properties of doped Nb₂O₅ systems and their related applications. Nb₂O₅ doped with Eu³⁺ exhibited strong emission at 610 nm with long decay times making it suitable for lighting devices.³⁵ Esteves *et al.* studied the effect of Mo and W doped Nb₂O₅ for the photooxidation of organic pollutants.³⁶

In view of the captivating features of doped systems, we have initially studied the changes in the physical and chemical properties of solution combustion synthesized Nb₂O₅ due to incorporation of metal dopants *viz.* Sr, Y, Zr, and Ag using characterization techniques such as XRD, XPS, SEM, TEM, and BET surface area measurements. We have especially emphasized on analysing the optical properties of pristine and metal-doped Nb₂O₅ such as narrowing of the band gap, band edge details, the presence of defects and charge carrier dynamics using DRS, UPS, PL, and TRF spectroscopy techniques. From the above analyses, the optimized concentration of these dopants in Nb₂O₅ was concluded and it was later validated experimentally from MB photodegradation. Next, we have checked the photoactivity of these materials over a wide range of water pollutants. To the best of our knowledge, this is the first time the effect of Sr, Y, Zr, and Ag doped Nb₂O₅ has been observed for the photocatalytic degradation of various dyes and organics as well as for the inactivation of bacteria. Further, kinetic studies for the degradation reactions and the scavenger test for determining the dominant reactive oxygen species (ROS) were also demonstrated. The reusability test of the catalyst was performed, and structural stability was confirmed from XRD analysis.

2 Experimental

2.1 Materials and methods

The metal oxide was prepared by the solution combustion technique which is considered a quick and efficient technique to yield nanoparticles with high phase purity.³⁷ A detailed procedure of preparing doped and pristine metal oxide by the solution combustion technique can be found elsewhere.²⁹ Ammonium niobate oxalate hydrate (Sigma-Aldrich, USA) was used as the precursor for niobium and urea as the fuel. All other chemicals used were of analytical grade. To prepare Nb₂O₅, initially, the niobium precursor and urea were dissolved in DI water separately *via* sonication for 10 min and later mixed together. The mixed clear solution was kept in a preheated muffle furnace at 450 °C for 30 min. Black Nb₂O₅ was obtained.³⁸ This catalyst was then calcined at 550 °C for 4 h to obtain white powdered pseudo hexagonal Nb₂O₅.³⁸ Metal nitrates were used as the precursors for dopants Sr, Y, Zr and Ag. The atomic doping percentages for metal doped niobia were varied in the range of 0.05–2.5% and the resulting compounds were termed Nb_(2-x)M_xO_{5-δ} where *x* is the dopant% and M is the dopant. For preparing the doped metal oxide the same procedure was used, in addition, the respective dopant's metal nitrate precursor was mixed with the sonicated niobium precursor urea solution.

2.2 Photochemical experiments

To check the photocatalytic activity of pristine and doped Nb₂O₅, MB, OG, IC were taken as model dye pollutants and 2-CP as model organic pollutant were taken as model pollutants. The photoreactor set up consisted of a metal halide lamp with an intensity of 121 W m⁻². The actinometry test was performed to check the lamp intensity and the methodology can be found elsewhere.³⁹ To avoid heating and maintain the reaction at 25 °C, the lamp was enclosed in a quartz jacket with inlet and outlet pipes connected to a chiller operating at 10 °C. The photodegradation experiments were performed in a quartz beaker. To attain an adsorption-desorption equilibrium, a 2 h dark reaction was performed before photocatalysis. Samples were collected at regular intervals, centrifuged and filtered for subsequent analysis. The degradation of the dyes was analyzed using UV-visible spectroscopy and the degradation of 2-CP was analyzed using HPLC (Waters Inc., USA). The system was equipped with a C-18 column with a UV detector and the mobile phase consisted of acetonitrile : water (20 : 80 v/v) with 0.01 M H₃PO₄ with a flow rate of 0.8 mL min⁻¹.

2.3 Photocatalytic inactivation of bacteria

E. coli strain K-12 MG1655 and *S. aureus* strain ATCC 259323 were taken as model organisms to check the antibacterial response of the photocatalysts. Glassware, micro-tips and other plastics used in the experiment were autoclaved at 120 °C for 2 h. The bacterial cells were incubated in Luria broth under constant agitation at 37 °C for 18 h. Later, the centrifuged washed clean bacterial pellet was suspended in 30 mL of sterile water with a final concentration of ~10⁸ CFU mL⁻¹. The



experiments were conducted under dark for 1 h followed by 1 h of light irradiation under a metal halide lamp with an intensity of 15 W m^{-2} . For analysis, $500 \mu\text{L}$ of the sample was collected at regular intervals of 20 min and the cell counting was done by the plate count method. The samples were serially diluted with sterile water and $50 \mu\text{L}$ of diluted samples were plated on solid nutrient agar plates. These plates were incubated at 37°C for 18 h. Subsequently, the number of viable cells was counted.

3 Characterization

XRD patterns were obtained using a Rigaku diffractometer using $\text{Cu-K}\alpha$ as a source of radiation. XPS of the materials were recorded using a Kratos Axis Ultra DLD instrument with monochromatic $\text{Al-K}\alpha$ X-rays as the energy source (1486 eV). UPS data were obtained using the same instrument with a helium-I source. UV-vis DRS data were obtained using a Shimadzu spectrophotometer (UV 2450). PL spectra of the catalysts were recorded using a PerkinElmer spectrophotometer. SEM, Carl Zeiss-Ultra 55 FESEM and TEM, Philips CM 200 were used to understand the surface morphology of the catalyst. BET surface area assessment was performed using a Smart Sorb 92/93 surface area analyzer. TRF data were obtained with a FLS 920 Spectrofluorometer (Edinburgh Instruments) using a laser diode for excitation.

4 Results and discussion

4.1 XRD analysis

To understand the phase purity of the prepared materials, XRD analysis was performed. In Fig. 1, the XRD diffraction patterns of pristine and doped Nb_2O_5 nanoparticles with 0.25 atom% metal ions (Sr, Y, Zr, and Ag) were compared. All the diffraction patterns correspond to the pure crystalline hexagonal Nb_2O_5 phase (JCPDS no. 28-0317) and no possible impurity phase was found in the samples. The predominant peak of Nb_2O_5 at $2\theta = 28.52^\circ$ corresponding to the (1 0 0) plane can be seen to shift to lower diffraction angles 28.27° , 28.35° , 28.43° and 28.34° when doped with Sr^{2+} , Y^{3+} , Zr^{4+} , and Ag^+ respectively. This can be attributed to the lattice strain generated due to larger ionic radii of the dopants as compared to Nb^{5+} .⁴⁰ The ionic radii of Nb^{5+} ,

Sr^{2+} , Y^{3+} , Zr^{4+} , and Ag^+ are 69 pm, 112 pm, 90 pm, 72 pm, and 126 pm respectively.⁴¹ The increase in the lattice parameters obtained from Rietveld refinement of the XRD patterns can be found in Table 1. These dopants substitute Nb^{5+} ions in their lattice sites causing a change in d -spacing and subsequently shifting XRD peaks to lower angles.⁴²

4.2 XPS analysis

XPS was performed to obtain the oxidation state of the elements present in the material. In Fig. 2(a) the peaks at binding energies 207.02 eV and 209.8 eV correspond to $\text{Nb-3d}_{5/2}$ and $\text{Nb-3d}_{3/2}$ with a spin-orbit splitting of 2.78 eV.⁴³ This confirms the element to be present in the +5 oxidation state. In Fig. 2(b) the peak at binding energy 529.9 eV can be assigned to lattice oxygen. The O-1s peak at 531.5 eV can be related to surface hydroxyl groups.⁴⁴ The XPS signals of the dopants were not detected due to their low atomic concentration.

4.3 UV-vis DRS

UV-vis DRS analysis can be utilized to compare the shift in the absorption spectra for pristine and doped Nb_2O_5 . Fig. S1(a)† shows the absorption spectra of Sr-doped Nb_2O_5 . It can be seen that with the increase in dopant concentration, the absorption edge of Nb_2O_5 was slightly red shifted, but as the dopant concentration was increased to 2.5%, the absorption edge tends to shift to a lower wavelength signifying an increase in the band gap. This could be due to the formation of a minute amount of strontium oxide. A similar trend was observed for Y and Zr doped Nb_2O_5 as shown in Fig. S1(b) and (c).† As known from the literature, strontium oxide, yttrium oxide and zirconium oxide are semiconductors with band gaps of 5.5 eV,⁴⁵ 5.17 eV (ref. 46) and 5 eV (ref. 47) respectively which are relatively higher than that of niobium oxide. Therefore, if the concentration of these dopants is increased beyond a certain limit, a minute formation of these oxides might occur on the surface of Nb_2O_5 causing a shift in the absorption edge of Nb_2O_5 to the lower wavelength region. However, silver oxide possesses a band gap of around 2.25 eV which is smaller than that of Nb_2O_5 ;⁴⁸ therefore from Fig. S1(d),† with the increase in Ag^+ concentration in Nb_2O_5 , the absorption edge was found to continue to shift to a higher wavelength even at a higher dopant concentration. From this analysis, it can be assumed that 0.25 atom% could be the optimized dopant concentration for Sr^{2+} , Y^{3+} , and Zr^{4+} in Nb_2O_5 , but for Ag^+ the optimized dopant concentration can be concluded from further analyses. However, experimentally from

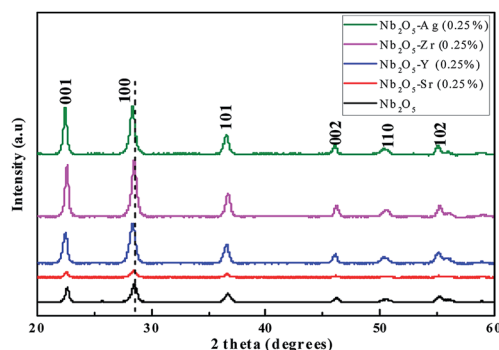


Fig. 1 XRD patterns of Nb_2O_5 doped with Sr, Y, Zr, and Ag of 0.25 atom%.

Table 1 Lattice parameters and particle size for pristine and doped Nb_2O_5

Catalyst	<i>a</i> (Å)	<i>b</i> (Å)	<i>c</i> (Å)	Band gap (eV)
Nb_2O_5	3.6115	3.6115	3.9269	3.00
$\text{Nb}_2\text{O}_5\text{-Sr}$ (0.25%)	3.6121	3.6121	3.9282	2.95
$\text{Nb}_2\text{O}_5\text{-Y}$ (0.25%)	3.6132	3.6131	3.9295	2.96
$\text{Nb}_2\text{O}_5\text{-Zr}$ (0.25%)	3.6216	3.6216	3.9396	2.94
$\text{Nb}_2\text{O}_5\text{-Ag}$ (0.25%)	3.6133	3.6133	3.9306	2.96





Fig. 2 XPS spectra of (a) Nb-3d and (b) O-1s.

MB degradation reactions in the photocatalysis section, Ag^+ at 0.1 atom% in Nb_2O_5 was found as the optimized dopant concentration.

To compare the band gaps of the different dopants in Nb_2O_5 with the optimized concentration, their absorbance spectra are shown in Fig. 3. The curve for doped Nb_2O_5 was red-shifted relative to pristine Nb_2O_5 from 417 nm to 420 nm, 422 nm, 423 nm and 427 nm due to the incorporation of Ag (0.1%), Y (0.25%), Sr (0.25%) and Zr (0.25%) dopants, respectively. This red shift suggests a slight reduction in the band gap of Nb_2O_5 . The optical band gap was obtained using the Tauc plot⁴⁹ ($F(R) \times h\nu$)^{1/n} vs. $h\nu$ as shown in the inset of Fig. 3. Here $h\nu$ is the photon energy in eV and $F(R)$ is the Kubelka–Munk function shown in eqn (1) which determines the extent of photon absorption of a semiconductor from its reflectance. From DFT studies, Nb_2O_5 was found to possess an indirect band gap;⁵⁰ therefore, n is taken to be 2 for indirect transitions.⁴⁹ From the Tauc plot, the

band gap (E_g) of the combustion synthesized Nb_2O_5 was found to be 3 eV and for doped Nb_2O_5 , a slight shift in the band gap was observed as shown in Table 1. The reduction in the band gap could be attributed to the insertion of Sr, Y, Zr or Ag cations into the Nb_2O_5 lattice. Since the conduction band minimum is made up of Nb 4d bands,⁵¹ the substitution of Nb^{5+} with these cations might induce their energy states to extend into the Nb_2O_5 conduction band, resulting in the narrowing of the band gap. The maximum reduction in the band gap was observed for Zr (0.25%) followed by Sr (0.25%), Y (0.25%) and Ag (0.1%). Decreasing the band gap helps the materials to absorb light in the visible region but this could also lead to faster recombination of charge carriers. Therefore, other parameters which are crucial for the photoactivity of a semiconductor such as BET surface area and lifetime of charge carriers are discussed in a later section.

$$F(R) = (1 - R)^2/2R \quad (1)$$



Fig. 3 UV-vis absorbance spectra of pristine and doped Nb_2O_5 and the inset presents the transformed Kubelka–Munk function vs. photon energy.

4.4 UPS analysis

The UPS technique can be employed to understand the valence band properties of a semiconductor. Fig. 4 presents the UPS spectrum of Nb_2O_5 where the peak at binding energy 14.8 eV was due to hybridization between O-2p and Nb-4d bonds. The peak at 12 eV is formed by the O-2p orbital. The peak at around 8 eV is from the O-2p in the valence band region. These analyses could be found elsewhere which were obtained by comparing the UPS spectrum with DOS results.⁵² UPS analysis can also be utilized to obtain the exact band edges of a semiconductor.⁵³ The work function (W_f) of a semiconductor surface is given by eqn (2) where $h\nu$ is the energy of photons from the Helium I source and SECO is the secondary electron cut off energy which is obtained from a linear extrapolation of the higher emission onset edge to zero intensity of higher binding energy.⁵⁴ Here $h\nu$ is 21.22 eV and SECO is 18.44 eV, and thus W_f is 2.78 eV. The





Fig. 4 UPS spectra of Nb₂O₅.

lower emission onset energy (E_2) is obtained by linear extrapolation of the intensity curve tangent to the baseline⁴⁹ and it is obtained at 4.2 eV. From DRS, the band gap of Nb₂O₅ is found to be 3 eV, and thus from eqn (3) and (4) the energy level of the valence band maximum (E_{vb}) is obtained at −6.98 V and the conduction band minimum (E_{cb}) at −3.98 V vs. Absolute vacuum scale (AVS).

$$W_f = 21.22 - \text{SECO} \quad (2)$$

$$E_{vb} = W_f + E_2 \quad (3)$$

$$E_{cb} = V_b - E_g \quad (4)$$

4.5 BET surface area

From BET surface area measurements shown in Table 2, it could be concluded that the surface area of Nb₂O₅ was enhanced when doped with Sr²⁺, Y³⁺, and Zr⁴⁺ metal ions. No significant variation in the surface area was observed from the increase in the dopant

concentration. However, for Ag⁺ doped Nb₂O₅, with the increase in the dopant concentration from 0.1% to 0.25%, the surface area increased by 1.4 times, but then decreased by 1.7 times when the concentration was increased to 2.5%. This could be due to agglomeration resulting in a decrease in the surface area.⁵⁵ On comparing the surface area of the dopants with the optimised dopant concentration in Nb₂O₅, the following trend can be concluded Sr (0.25%) > Zr (0.25%) > Y (0.25%) > Ag (0.1%). Along with the increase in the surface area, analysis of the lifetime of charge carriers is important for determining the photoactivity of the material as these parameters need not be directly proportional to each other. To determine the presence of defects and recombination time of excitons, PL and TRF analyses are discussed in later sections.

4.6 PL analysis

From photoluminescence analysis, information on the photochemical properties of a semiconductor such as oxygen vacancies, defects, and charge carrier transfer can be obtained.⁵⁶ Nb₂O₅ with an excitation wavelength of 325 nm was found to exhibit photoluminescence in the range from 350 to 550 nm as shown in Fig. 5. The short wavelength emissions at 409 nm can be attributed to the near band edge emissions where electron transitions take place from the bottom of the conduction band to the top of the valence band.⁵⁶ The emission spectra at 448, 466, 480, 490 and 560 nm can be related to surface defects and oxygen vacancies^{56,57} where transitions occur in the energy levels within the band gap.⁵⁸ No new PL signal was observed from the doped metals but variation in intensity was found. The intensities of Zr (0.25%) and Y (0.25%) doped Nb₂O₅ were found to be higher than that of Nb₂O₅. This could be due to the higher content of surface defects and oxygen vacancies that are the source of non-radiative recombination⁵⁸ and possibly not due to the higher recombination rate as evident from the recombination time of charge carriers from TRF analysis. The intensities of Sr (0.25%) and Ag (0.1%) doped Nb₂O₅ were found to be lower

Table 2 BET surface area and TRF charge carrier dynamics of doped and pristine Nb₂O₅, and the rate constant of MB photodegradation

Catalyst	BET surface area (±1 m ² g ^{−1})	Lifetime of charge carriers τ_{avg} (ps)	MB adsorption rate constant k_a (±0.1 h ^{−1})	MB photodegradation rate constant k_m (±0.05 h ^{−1})
Photolysis	—	—	—	0.01
Nb ₂ O ₅	28	1088	1.6	0.19
Nb ₂ O ₅ –Sr (0.1%)	32	1223	—	0.42
Nb ₂ O ₅ –Sr (0.25%)	43	1290	2.3	0.60
Nb ₂ O ₅ –Sr (2.5%)	44	1212	—	0.41
Nb ₂ O ₅ –Y (0.1%)	38	1047	—	0.30
Nb ₂ O ₅ –Y (0.25%)	36	1241	2.2	0.49
Nb ₂ O ₅ –Y (2.5%)	33	1127	—	0.46
Nb ₂ O ₅ –Zr (0.1%)	36	1143	—	0.43
Nb ₂ O ₅ –Zr (0.25%)	38	1162	2.4	0.54
Nb ₂ O ₅ –Zr (2.5%)	41	904	—	0.42
Nb ₂ O ₅ –Ag (0.1%)	32	1202	2.3	0.58
Nb ₂ O ₅ –Ag (0.25%)	45	1029	—	0.47
Nb ₂ O ₅ –Ag (2.5%)	26	1084	—	0.40



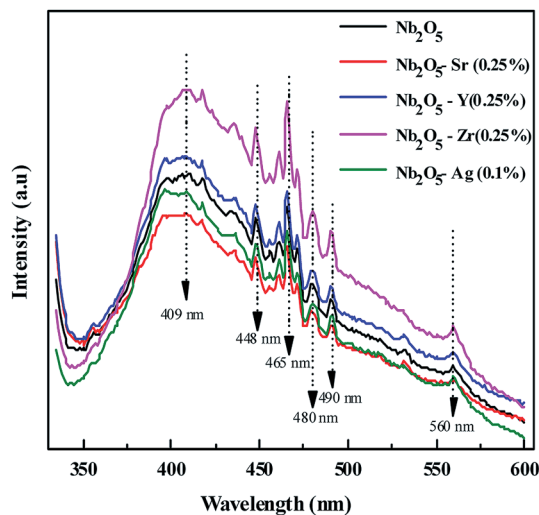


Fig. 5 PL spectra of the doped and pristine Nb_2O_5 .

signifying a lower recombination rate of excitons than that of Nb_2O_5 .

4.7 Charge carrier dynamics by TRF analysis

The lifetime of charge carriers can be obtained from TRF analysis. The lifetime emission decays of pristine and metal-doped Nb_2O_5 spectra were measured at a maximum emission wavelength of 415 nm (as obtained from PL analysis) using a 305 nm laser diode. Fig. 6 shows the TRF decay curve for Nb_2O_5 . The decay curve was fitted using a two parameter biexponential decay model (eqn (5)) with R^2 higher than 0.97. Here A_1 and A_2 are the decay constants; the shorter lifetime τ_1 corresponds to the non-radiative process which is due to heat losses and the longer lifetime τ_2 corresponds to the radiative process which provides information related to the electron-hole recombination.⁵⁹ The average lifetime was calculated using eqn

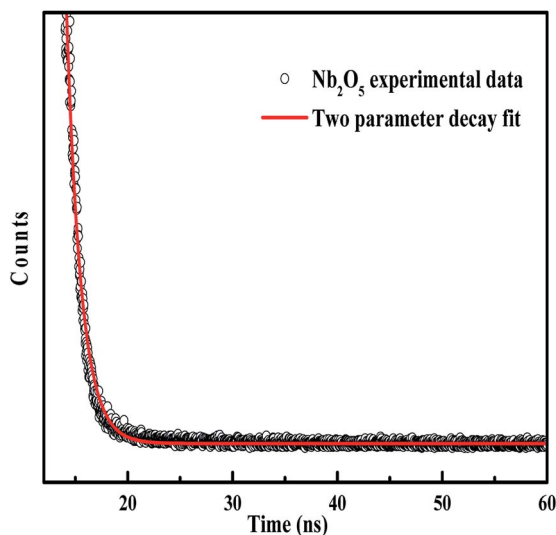


Fig. 6 TRF decay curve of Nb_2O_5 .

(6).⁶⁰ The lifetime of charge carriers (τ_{avg}) is shown in Table 2. For Nb_2O_5 , τ_{avg} was found to be 1088 picoseconds (ps) and with the incorporation of dopants into the host Nb_2O_5 , the lifetime of charge carriers was found to have increased. Indeed Sr (0.25%), Y (0.25%), Zr (0.25%) and Ag (0.1%) were found to have a longer lifetime compared to 0.1% and 2.5% dopant concentration. With the excess dopant concentration of 2.5%, τ_{avg} decreased as the increased dopant concentration must have acted as the recombination centers.⁶¹ On comparing the lifetimes of optimised dopants the following trend can be observed $\text{Sr (0.25\%)} > \text{Y (0.25\%)} > \text{Zr (0.25\%)} > \text{Ag (0.1\%)}$. The significance of the longer lifetime of charge carriers vs. the photoactivity of the catalysts towards different pollutants is discussed in the photocatalysis section.

$$y = A_1 \exp(-t/\tau_1) + A_2 \exp(-t/\tau_2) \quad (5)$$

$$\tau_{\text{avg}} = (A_1 \times \tau_1^2 + A_2 \times \tau_2^2) / (A_1 \times \tau_1 + A_2 \times \tau_2) \quad (6)$$

4.8 SEM and TEM analysis

Fig. 7(a) and (b) show the SEM images of Nb_2O_5 and Sr (0.25%) doped Nb_2O_5 nanoparticles which are found to have an earth rock like structure. No specific morphology change was observed due to the incorporation of dopants. The SEM images for the other doped materials are shown in Fig. S2(a)–(c).† The d spacings of 3.0 Å and 3.9 Å obtained from the HR TEM images in Fig. 7(c) and (d) correspond to planes (1 0 0) and (0 0 1) respectively, and the inset shows the FFT images. These planes with the respective d spacing can be validated from the XRD patterns.

4.9 Photocatalysis

4.9.1 MB photo degradation

4.9.1.1 Effect of catalyst loading. The degradation of MB was evaluated by monitoring the decrease in the absorbance peak at 665 nm using UV-visible spectroscopy. Fig. S3 in the ESI† presents the effect of catalyst loading for the degradation of MB with an initial concentration of 15 ppm. The experiment was carried out at a neutral pH of 7. The zero-point charge (pH_{zpc}) of Nb_2O_5 (as obtained from the pH drift method⁶²) is 4, as shown in Fig. S4.† The surface of Nb_2O_5 is positively charged at pH below pH_{zpc} and negatively charged at pH above pH_{zpc} .⁵³ Therefore, MB which is a cationic dye gets adsorbed readily on the surface of Nb_2O_5 at pH 7. For control, photolysis was performed which showed no degradation of the dye. The adsorption-desorption equilibrium for the catalyst was achieved in 2 h of reaction under dark conditions. A catalyst loading of 0.2 g L^{-1} degraded the dye by 20% at the end of 2 h. This lower catalyst loading was not sufficient to generate enough ROS to degrade the dye. A loading of 0.5 g L^{-1} degraded the dye by 46%. On further increasing the catalyst loading to 1 g L^{-1} , the solution became turbid. This hindered the penetration of light which resulted in a decrease in activity, thereby degrading the dye by 44% at the end of 2 h.⁶³ Therefore, 0.5 g L^{-1} was taken as the optimum catalyst loading to perform further experiments.



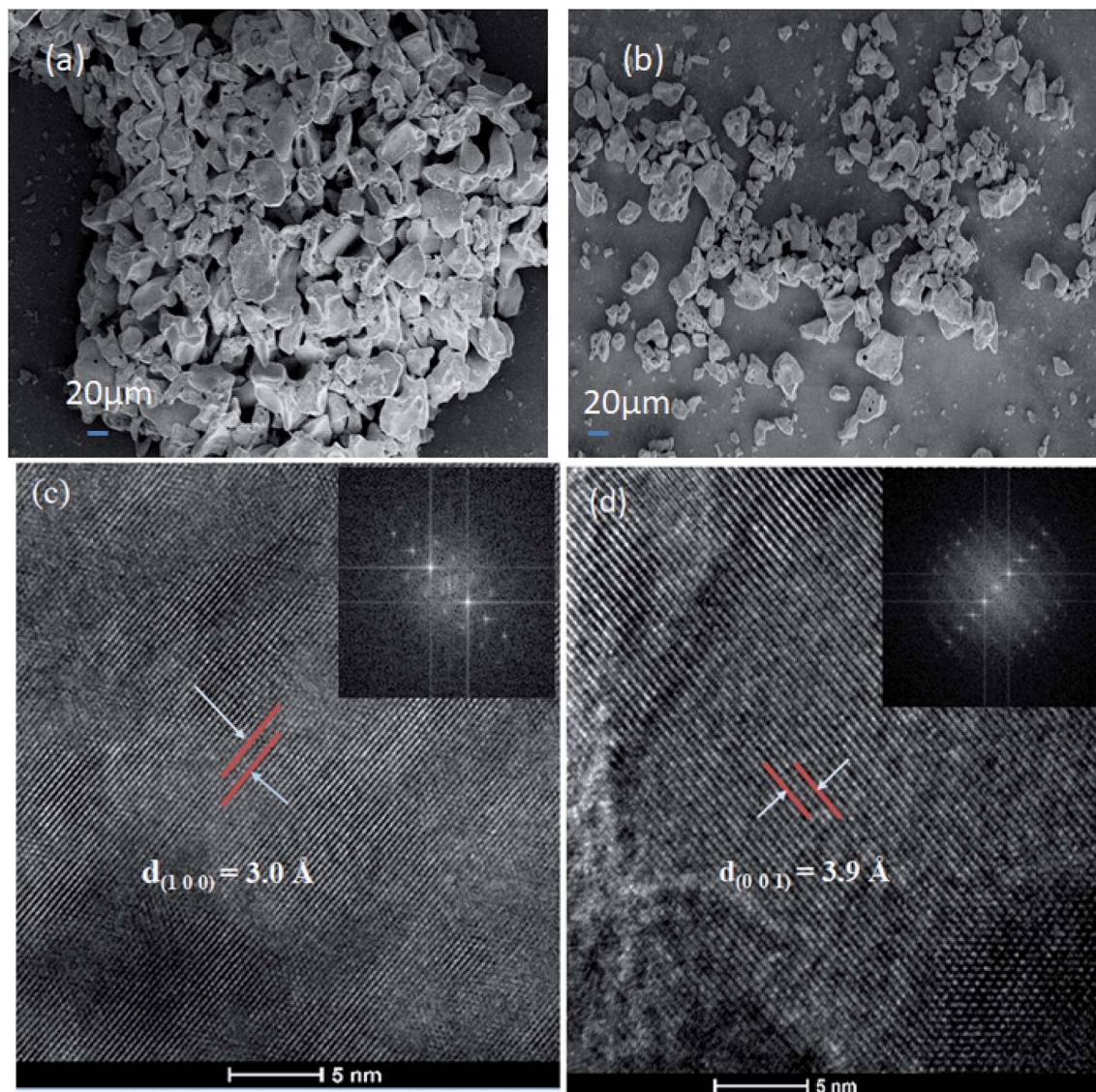


Fig. 7 (a) SEM image of Nb₂O₅, (b) SEM image of Sr (0.25%)–Nb₂O₅, (c) HRTEM image of Nb₂O₅ showing the *d* spacing of the (1 0 0) plane and the inset shows the FFT image, and (d) HRTEM image of Nb₂O₅ showing the *d* spacing of the (0 0 1) plane and the inset presents the FFT image.

4.9.1.2 Optimization of Sr, Y, Zr and Ag concentration doped in Nb₂O₅ towards MB degradation. To inhibit charge carrier recombination, optimization of dopant concentration is necessary for achieving higher photocatalytic activity.³⁰ Fig. S5(a)† shows the effect of Sr doping concentration in Nb₂O₅ for MB photodegradation. Sr content at 0.25% was found to be the optimized concentration and the same was observed for Y and Zr doped Nb₂O₅ from Fig. S5(b) and (c).† This could be attributed to the greater number of active sites at this dopant concentration as evident from 2 h of dark adsorption. As the dopant concentration was increased to 2.5%, the photocatalytic activity for all the above dopants decreased which is also complemented by TRF analysis. The reduction in the distance between the trap sites resulted in faster electron–hole recombination as the excess dopant concentration acted as the recombination centers.⁶¹ For Ag-doped Nb₂O₅ the optimized

dopant loading was 0.1%, as shown in Fig. S5(d).† When the loading increased beyond the optimal level, reduction in the activity could be due to faster recombination. Therefore, when Ag loading is increased, clusters of Ag species form overlapping agglomerates which shadow the photocatalytic activity due to surface plasmon absorption.⁶⁴

4.9.1.3 Rate kinetics for MB adsorption and photodegradation using optimized dopant concentration. The adsorption of MB on metal doped Nb₂O₅ shown in Fig. S6† was found to follow Lagergren's pseudo-first-order reaction model (eqn (7)), where k_a is the adsorption rate constant (h^{-1}) and q_e and q_t are the amounts of adsorbed dye (mg g^{-1}) at equilibrium and at time t .⁶⁵ Following adsorption, the photodegradation of MB shown in Fig. 8 followed the Langmuir–Hinshelwood model (eqn (8)).⁶⁶ Here k_m is the photodegradation rate constant and

$$\ln(q_e - q_t) = \ln(q_e) - k_a t \quad (7)$$





Fig. 8 Effect of dopants in Nb_2O_5 for MB degradation and the inset represents rate kinetics.



Fig. 9 Effect of dopants in Nb_2O_5 for OG degradation and the inset presents rate kinetics.

$$\ln(C_0/C) = k_{\text{m}}t + \ln(C_0/C_1) \quad (8)$$

C_0 is the initial dye concentration. C_1 and C are the concentrations at reaction time zero and at time t . The rate constants

for MB adsorption and photodegradation kinetics are shown in Table 2. The rate constants for photodegradation of the dye were found to follow the order $\text{Sr} > \text{Ag} > \text{Zr} > \text{Y}$. However, from TRF analysis, the lifetime of the charge carriers followed the order $\text{Sr} > \text{Y} > \text{Ag} > \text{Zr}$. The non-complementary relation between the photoactivity and the lifetime of charge carriers could be the presence of deep trap states in the catalyst. The electrons trapped in these states show a longer lifetime but are unable to reduce electron acceptors, thus lowering the efficiency of photocatalytic reactions.⁶⁷ The number of active sites for adsorption, increase in surface area and the lifetime of charge carriers all play roles in degrading the pollutant. It would be difficult to identify the dominant property of the material for the activity towards pollutant degradation.

4.9.2 OG photodegradation: effect of pH and dopants. The initial concentration of OG was taken as 20 ppm. The photodegradation of the dye was monitored by checking the absorbance at 480 nm using UV-vis spectroscopy. OG is an anionic dye and at a neutral pH of 7.6, with an optimized catalyst loading of 1.2 g L^{-1} (Fig S7†), the dye was degraded only by 2% as seen from Fig. S8.† With the decrease in pH, the degradation increased. A maximum degradation of 30% was observed at pH 3.25. However, at a very low pH of 2.5, the catalyst surface was masked by a greater number of H^+ adsorbing on it, preventing the photoexcitation of Nb_2O_5 and leading to a decrease in the photocatalytic activity. Similar phenomena were observed in some other studies.⁶⁸

Fig. 9 presents the photodegradation profile of OG with Nb_2O_5 doped with Sr, Y, Zr, and Ag with the optimized concentration of the dopants at pH 3.25 and a loading of 1.21 g L^{-1} . No significant discoloration of the dye was observed in 2 h of dark reaction. For control, photolysis was performed which showed no degradation of the dye. The doped material was found to perform better than pristine Nb_2O_5 following the order $\text{Sr} > \text{Zr} \sim \text{Y} > \text{Ag} > \text{pristine Nb}_2\text{O}_5$. This order could be attributed to the same increasing trend in the surface area of the doped catalyst. The photodegradation of OG was found to follow 1st order kinetics (eqn (9)), where k_0 is the rate constant, C_0 is the initial concentration and C is the concentration at time t . The rate constants are shown in Table 3.

$$\ln(C/C_0) = -k_0t \quad (9)$$

Table 3 Rate constants for OG, IC, 2-CP, *E. coli* and *S. aureus* inactivation

Catalyst	OG degradation rate constant k_0 ($\pm 0.01 \text{ h}^{-1}$)	IC degradation rate constant k_i ($\pm 0.01 \text{ h}^{-1}$)	2-CP degradation rate constant k_c ($\pm 0.01 \text{ h}^{-1}$)	<i>E. coli</i> inactivation rate constant k_e ($\pm 0.01 \text{ min}^{-1}$)	<i>S. aureus</i> inactivation rate constant k_s ($\pm 0.005 \text{ min}^{-1}$)
Photolysis	0.008	0.14	0.04	0.027	0.008
Nb_2O_5	0.134	0.29	0.13	0.076	0.019
$\text{Nb}_2\text{O}_5\text{-Sr}$ (0.25%)	0.201	1.11	0.58	0.120	0.069
$\text{Nb}_2\text{O}_5\text{-Y}$ (0.25%)	0.178	0.37	0.49	0.098	0.028
$\text{Nb}_2\text{O}_5\text{-Zr}$ (0.25%)	0.172	0.52	0.50	0.115	0.053
$\text{Nb}_2\text{O}_5\text{-Ag}$ (0.1%)	0.138	0.35	0.44	0.118	0.051



4.9.3 IC photodegradation. The initial concentration of IC was taken as 40 ppm. The photodegradation of the dye was monitored by checking the absorbance at 610 nm using UV-vis spectroscopy. Since IC is also an anionic dye, no degradation of the dye was observed at a neutral pH of 7.5. From Fig. S9,† around maximum degradation of the dye was observed at pH 3 with a catalyst loading of 0.5 g L⁻¹. The doped materials were found to perform better than pristine Nb₂O₅, Fig. 10 following the order Sr > Zr > Y > Ag > pristine Nb₂O₅ following 1st order kinetics (eqn (10)) with a maximum degradation of 95% from Sr (0.25%) doped Nb₂O₅ where k_i is the rate constant for IC photodegradation. The rate constants are shown in Table 3.

$$\ln(C/C_0) = -k_i t \quad (10)$$

4.9.4 2-CP photodegradation. The photodegradation of 2-CP was analyzed using HPLC with an initial concentration of 25 ppm. The adsorption-desorption equilibrium was observed in 2 h of dark reaction. Fig. 11 presents the effect of pristine and doped Nb₂O₅ for 2-CP photodegradation and the inset presents the rate kinetics. Around 90% degradation of the pollutant was observed from the doped catalysts as compared to 15% degradation from photolysis and around 50% from pristine Nb₂O₅. The photodegradation followed 1st order kinetics (eqn (11)), where k_p is the rate constant at a neutral pH of 7.3 and a catalyst loading of 0.5 g L⁻¹. The rate constants are shown in Table 3 following the order Sr > Zr > Y > Ag > Nb₂O₅.

$$\ln(C/C_0) = -k_p t \quad (11)$$

4.9.5 Antibacterial experiments. To assess the antibacterial response of the catalysts, *E. coli* was taken as a model Gram-negative bacterium. Fig. S10† presents the effect of catalyst

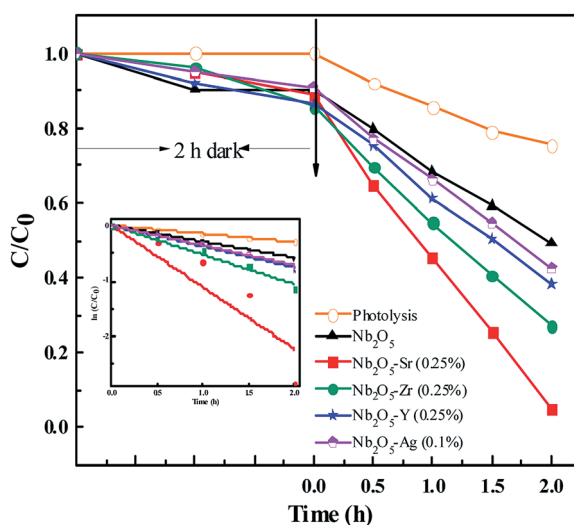


Fig. 10 Effect of dopants in Nb₂O₅ for IC degradation and the inset presents rate kinetics.

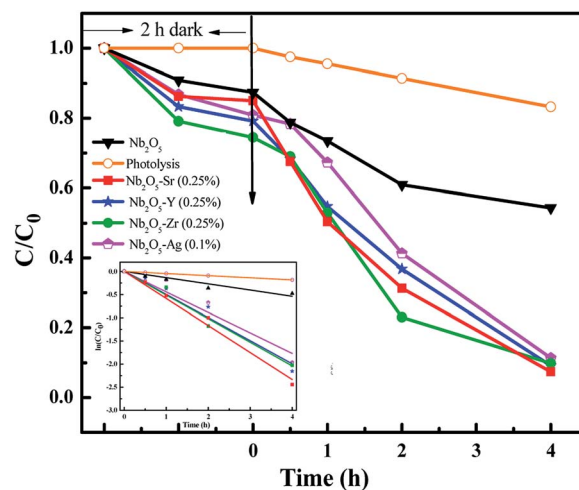


Fig. 11 Effect of dopants in Nb₂O₅ for 2-CP degradation and the inset presents rate kinetics.

loading using Sr (0.25%) doped Nb₂O₅ as a catalyst for the photoinactivation of *E. coli*. The initial bacterial concentration was taken as 2×10^8 CFU mL⁻¹. It was observed that a loading of 0.05 g L⁻¹ was too low to inactivate bacteria and 0.25 g L⁻¹ caused turbidity causing a decrease in the rate of inactivation. The optimized loading was found to be 0.1 g L⁻¹ resulting in a 3.5 log reduction of *E. coli* cells. Fig. 12 shows the effect of different dopants in Nb₂O₅ for *E. coli* photoinactivation and the inset presents the rate kinetics. For control, photolysis was performed and less than 1-log reduction was observed. A 1.5-log reduction in bacterial cells was observed with Nb₂O₅. The doped material was found to perform better than Nb₂O₅ with rate constants following the order Sr ~ Zr ~ Ag > Y > Nb₂O₅. Around 3.5 log reduction was observed from Ag, Zr and Sr-doped Nb₂O₅ and a 3-log reduction was found from Y doped Nb₂O₅. However, when a model Gram-positive strain *S. aureus* was taken with an initial count of 10^8 CFU mL⁻¹, the bactericidal efficacy was



Fig. 12 Effect of dopants in Nb₂O₅ for *E. coli* inactivation and the inset presents rate kinetics.



maximum of ~ 2 log fold from Sr doped Nb_2O_5 as shown in Fig. 13. From photolysis, insignificant reduction in *S. aureus* cells was observed and around 0.5 log reduction from pristine Nb_2O_5 . Since the major bacterial contamination pertaining in the domestic water system is by fecal coliforms and not predominantly due to Gram-positive species,^{4,69} our catalyst can remediate water effectively. The photoinactivation of *E. coli* and *S. aureus* was found to follow 1st order kinetics fitting the data using eqn (12) and (13) where k_e and k_s are the rate constants for *E. coli* and *S. aureus*, respectively, C_0 is the initial concentration and C is the concentration at time t . The rate constants are shown in Table 3.

$$\ln(C/C_0) = -k_e t \quad (12)$$

$$\ln(C/C_0) = -k_s t \quad (13)$$

4.10 Scavenger test

To identify the active species taking part in the photo-degradation reactions, trapping experiments were carried out. MB and *E. coli* were taken as the test pollutants and Sr (0.25%) doped Nb_2O_5 as the catalyst. 1 mM *t*-butanol,⁷⁰ 1 mM EDTA-Na⁷⁰ and 2 mM TEMPO⁷¹ were used as scavengers for OH , h^+ and $\text{O}_2^{\cdot-}$ radicals respectively in the photoreaction containing the dye/*E. coli* and the catalyst in the presence of light. Control experiments included reaction in the presence of scavengers, dye/*E. coli* and light without the catalyst and it was observed that there was insignificant dye degradation or bacterial inactivation from Fig. 14 and S11.† The main active species identified were superoxide radicals suppressing the degradation rate of the dye by $\sim 60\%$. Generation of superoxide radicals at -4.17 V vs. the AVS scale was evident from UPS analysis. The holes were also capable of directly oxidizing the pollutant as the scavenger EDTA could prevent the dye degradation by 40%. In the case of antibacterial experiments as well, superoxide radicals and holes were found to be the main active

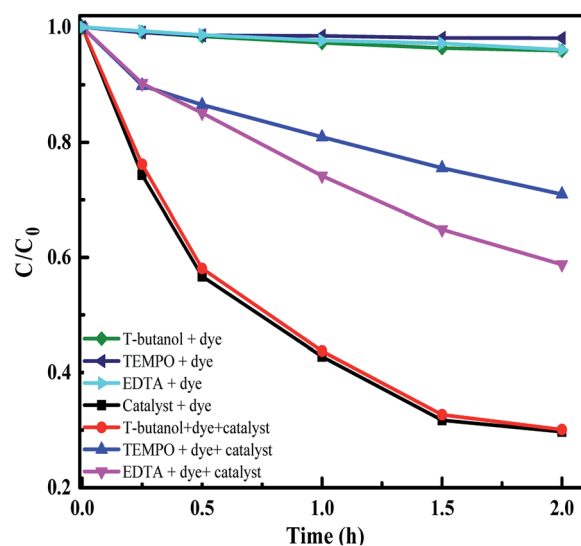


Fig. 14 Radical trapping experiment with scavengers and MB as the pollutant.

species. Scavengers TEMPO and EDTA were found to suppress the inactivation by almost 90%.

4.11 Proposed mechanism

A possible mechanism is proposed using the combined analysis from PL, DRS, UPS, TRF and scavenger tests. A schematic of such a mechanism with energy levels of Nb_2O_5 is shown in Fig. 15. The as-prepared Nb_2O_5 nanoparticles were found to absorb in the near visible region with a band gap E_g of 3 eV and the energy level of the conduction band minimum E_{cb} at -3.98 V and that of the valence band maximum E_{vb} at -6.98 V vs. AVS. The conduction band of Nb_2O_5 is made up of Nb-4d orbitals and the valence band consists of O-2p orbitals.⁵¹ When photons ($h\nu$) with energy equal to or greater than 3 eV are incident on Nb_2O_5 , electronic transitions can take place from E_{vb} to E_{cb} of the semiconductor or to the defect states. The presence of defects in the Nb_2O_5 semiconductor was detected from PL analysis, generated due to the presence of vacancies, impurities or interstitial atoms.⁷² These defects lying near E_{cb} or E_{vb} can capture the electrons or the holes evading charge recombination. Also, incorporation of dopants induces their own energy states in the semiconductor which captures the photoinduced electrons. This enhances charge separation resulting in prolonged recombination time as validated from TRF analysis. The orbitals of the dopants Sr, Y, Zr, and Ag could be lying around or merging with the Nb-4d orbitals of Nb_2O_5 as a slight reduction in the band gap of Nb_2O_5 was observed on doping. These trapped electrons or the electrons in E_{cb} can react with oxygen to produce $\text{O}_2^{\cdot-}$ radicals which are the main active species responsible for organic pollutant photodegradation as well as for bacterial inactivation. The other active species as evident from scavenger experiments are the positive holes which are created in the E_{vb} or the trapped holes that could directly attack the pollutants.⁷³

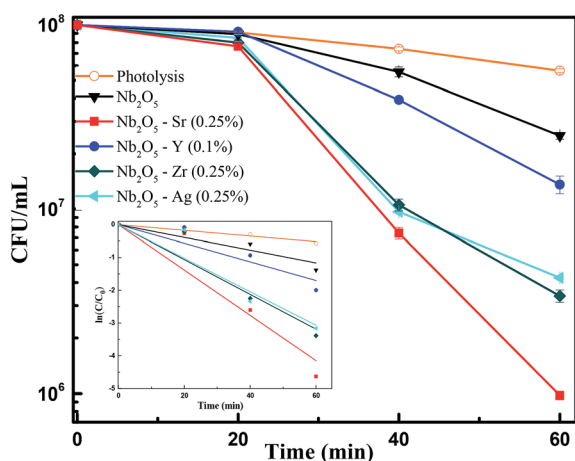


Fig. 13 Effect of dopants in Nb_2O_5 for *S. aureus* inactivation and the inset represents rate kinetics.



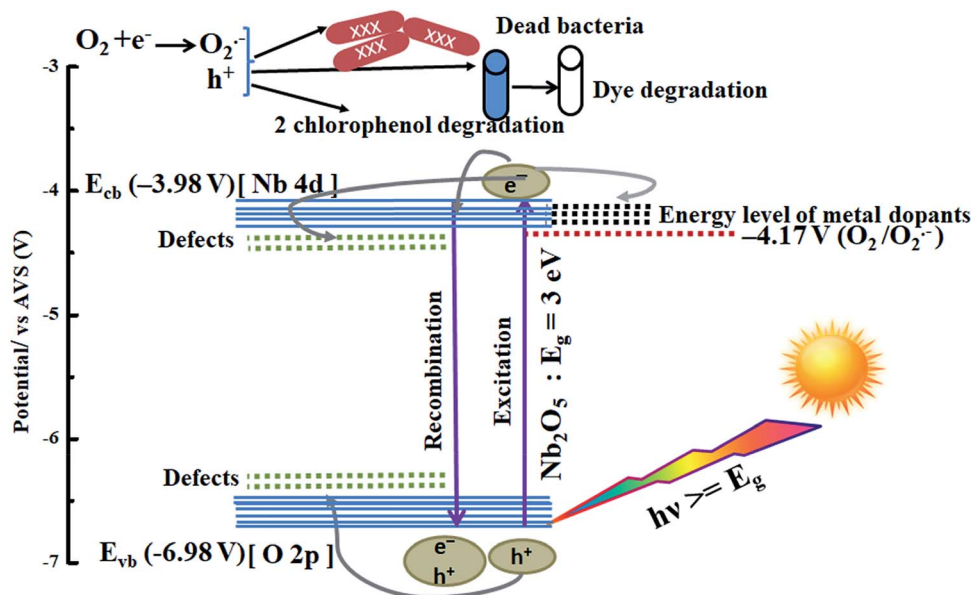


Fig. 15 Photocatalysis mechanism in metal-doped Nb_2O_5 .

4.12 Reusability and structural stability

Fig. S12[†] shows the reusability of the Sr 0.25% doped Nb_2O_5 catalyst for the degradation of MB. After five cycles the catalyst could degrade the dye by 70%, and the activity was found to decrease only by 12.5% compared to the fresh catalyst. Fig. S13[†] shows the XRD pattern of the catalyst before and after use for 5 cycles. No change in the pattern was observed confirming its stability.

5 Conclusions

This study presents the optical and photocatalytic properties of solution combustion synthesized Nb_2O_5 nanoparticles. The derived photocatalyst exhibited a band gap of 3 eV with a valence band edge at -6.98 V and conduction band edge at -3.98 V vs. AVS signifying the energy level to be sufficient enough to generate superoxide radicals at -0.417 V. The work function of the material was found to be 2.78 eV. Several properties of this host material were influenced on doping with metals (Sr, Y, Zr, and Ag) such as increment in the lattice parameters as analyzed from Rietveld refinement of the XRD patterns of pristine and doped Nb_2O_5 , and enhancement in the surface area from BET analysis. A red shift in the absorption edge of Nb_2O_5 on doping was found from DRS analysis. The as-prepared niobium oxide was found to have surface defects and oxygen vacancies from PL analysis. Doping Nb_2O_5 with metals facilitated better charge separation and the optimized concentrations of dopants Sr^{2+} , Y^{3+} and Zr^{4+} were found to be 0.25% and 0.1% for the Ag^+ dopant from the TRF technique. The optimization of this dopant concentration was also validated experimentally by analyzing MB photodegradation. The doped materials showed excellent photoactivity towards dye and chlorophenol degradation as well as bacterial inactivation. The affinity of these materials

towards the degradation of each pollutant was different, but Sr (0.25%) doped Nb_2O_5 was found to be the best amongst all the other catalysts. From the scavenger test, superoxide radicals and holes were found to be the dominant reactive oxygen species in the photodegradation reactions. The catalyst was found to be stable after 5 cycles and the structural stability was confirmed from XRD analysis. This study suggests that combustion synthesized Sr (0.25%) doped Nb_2O_5 is chemically stable and could be used as a potential photocatalyst for antimicrobial action and degradation of recalcitrant organic contaminants.

Conflicts of interest

There are no conflicts to declare.

Acknowledgements

The authors would like to thank the Department of Science and Technology (DST), India for financial support. The authors thank the IPC and CeNSE for characterization facilities, the Centre for Earth Science, IISc for ICP-MS analysis and the SSCU for DRS and PL facility. The authors are grateful to Prof. Anshu Pandey for TRF facility and Mr Paresch Samantaray for SEM imaging.

References

- 1 P. K. Samantaray, S. Baloda, G. Madras and S. Bose, *Adv. Sustainable Syst.*, 2019, 1800153.
- 2 C. A. Martínez-Huitle and E. Brillas, *Appl. Catal., B*, 2009, **87**, 105–145.
- 3 N. Rao, A. Dubey, S. Mohanty, P. Khare, R. Jain and S. Kaul, *J. Hazard. Mater.*, 2003, **101**, 301–314.



- 4 P. K. Samantaray, G. Madras and S. Bose, *ChemistrySelect*, 2017, **2**, 7965–7974.
- 5 P. K. Samantaray, G. Madras and S. Bose, *ACS Sustainable Chem. Eng.*, 2018, **7**, 1580–1590.
- 6 V. Gupta, *J. Environ. Manage.*, 2009, **90**, 2313–2342.
- 7 M. R. Gadekar and M. M. Ahammed, *Desalin. Water Treat.*, 2016, **57**, 26392–26400.
- 8 P. K. Samantaray, G. Madras and S. Bose, *J. Membr. Sci.*, 2018, **548**, 203–214.
- 9 S. Raghu and C. A. Basha, *J. Hazard. Mater.*, 2007, **149**, 324–330.
- 10 V. Lazarova, P. Savoye, M. Janex, E. Blatchley Iii and M. Pommepuy, *Water Sci. Technol.*, 1999, **40**, 203–213.
- 11 S. Bose and P. Samantaray, *Proc. Indian Natl. Sci. Acad.*, 2018, **84**, 669–679.
- 12 J. Chapman, F. Regan and T. Sullivan, *Nanoparticles in Antimicrobial Materials: Use and Characterisation*, Royal Society of Chemistry, 2012.
- 13 N. Padmavathy, P. K. Samantaray, L. D. Ghosh, G. Madras and S. Bose, *Nanoscale*, 2017, **9**, 12664–12676.
- 14 J.-M. Herrmann, C. Guillard and P. Pichat, *Catal. Today*, 1993, **17**, 7–20.
- 15 A. Fujishima, X. Zhang and D. A. Tryk, *Surf. Sci. Rep.*, 2008, **63**, 515–582.
- 16 P. A. Pekakis, N. P. Xekoukoulotakis and D. Mantzavinos, *Water Res.*, 2006, **40**, 1276–1286.
- 17 K. M. Lee, C. W. Lai, K. S. Ngai and J. C. Juan, *Water Res.*, 2016, **88**, 428–448.
- 18 A. Fujishima and X. Zhang, *C. R. Chim.*, 2006, **9**, 750–760.
- 19 O. Ola and M. M. Maroto-Valer, *J. Photochem. Photobiol., C*, 2015, **24**, 16–42.
- 20 C. Gadiyar, B. Boruah, C. Mascarenhas and V. Shetty, *Int. J. Res. Eng. Technol.*, 2013, 2277–4106.
- 21 A. G. Prado, L. B. Bolzon, C. P. Pedroso, A. O. Moura and L. L. Costa, *Appl. Catal., B*, 2008, **82**, 219–224.
- 22 A. Mozalev, M. Bendova, R. Vazquez, Z. Pytlicek, E. Llobet and J. Hubalek, *Sens. Actuators, B*, 2016, **229**, 587–598.
- 23 M. Zhang, H. Wen, J. Yu, F. Ai, H. Yu, X. Pan, H. Shao, M. Tang and L. Gai, *Opt. Mater. Express*, 2017, **7**, 3222–3230.
- 24 Y. Zhao, C. Ding, Y. Hao, X. Zhai, C. Wang, Y. Li, J. Li and H. Jin, *ACS Appl. Mater. Interfaces*, 2018, **10**, 27106–27115.
- 25 S. Furukawa, T. Shishido, K. Teramura and T. Tanaka, *ChemPhysChem*, 2014, **15**, 2665–2667.
- 26 X. Chen, T. Yu, X. Fan, H. Zhang, Z. Li, J. Ye and Z. Zou, *Appl. Surf. Sci.*, 2007, **253**, 8500–8506.
- 27 R. Asahi, T. Morikawa, T. Ohwaki, K. Aoki and Y. Taga, *Science*, 2001, **293**, 269–271.
- 28 K. Wilke and H. Breuer, *J. Photochem. Photobiol., A*, 1999, **121**, 49–53.
- 29 R. Gupta, N. K. Eswar, J. M. Modak and G. Madras, *RSC Adv.*, 2016, **6**, 85675–85687.
- 30 Y. Ma, J. Zhang, B. Tian, F. Chen and L. Wang, *J. Hazard. Mater.*, 2010, **182**, 386–393.
- 31 S. Sood, A. Umar, S. K. Mehta, A. Sinha and S. K. Kansal, *Ceram. Int.*, 2015, **41**, 3533–3540.
- 32 N. Xinshu, L. Sujuan, C. Huihui and Z. Jianguo, *J. Rare Earths*, 2011, **29**, 225–229.
- 33 X. Lei, X. Xue and H. Yang, *Appl. Surf. Sci.*, 2014, **321**, 396–403.
- 34 S.-m. Chang and R.-a. Doong, *J. Phys. Chem. B*, 2006, **110**, 20808–20814.
- 35 D. Falcomer, A. Speghini, G. Ibba, S. Enzo, C. Cannas, A. Musinu and M. Bettinelli, *J. Nanomater.*, 2007, **2007**, 94975.
- 36 A. Esteves, L. C. Oliveira, T. C. Ramalho, M. Goncalves, A. S. Anastacio and H. W. Carvalho, *Catal. Commun.*, 2008, **10**, 330–332.
- 37 T. Mimani and K. Patil, *Mater. Phys. Mech.*, 2001, **4**, 134–137.
- 38 S. Li, Q. Xu, E. Uchaker, X. Cao and G. Cao, *CrystEngComm*, 2016, **18**, 2532–2540.
- 39 R. Gupta, B. Boruah, J. M. Modak and G. Madras, *J. Photochem. Photobiol., A*, 2019, **372**, 108–121.
- 40 V. Morris, R. Farrell, A. Sexton and M. Morris, 2006.
- 41 S. Ruben, *Handbook of the Elements*, Open Court, 1985.
- 42 D. P. Dutta, M. Ramakrishnan, M. Roy and A. Kumar, *J. Photochem. Photobiol., A*, 2017, **335**, 102–111.
- 43 J.-H. Jang, T.-Y. Kim, N.-J. Kim, C.-H. Lee, E.-M. Park, C. Park and S.-J. Suh, *Mater. Sci. Eng., B*, 2011, **176**, 1505–1508.
- 44 A. Naldoni, M. Allieta, S. Santangelo, M. Marelli, F. Fabbri, S. Cappelli, C. L. Bianchi, R. Psaro and V. Dal Santo, *J. Am. Chem. Soc.*, 2012, **134**, 7600–7603.
- 45 S. Stankic, J. Bernardi, O. Diwald and E. Knözinger, *J. Phys. Chem. C*, 2007, **111**, 8069–8074.
- 46 G. Bhavani, S. Ganesan, S. Selvasekarapandian, S. Monisha and M. Premalatha, *Ionics*, 2016, **22**, 581–592.
- 47 C. Gionco, M. C. Paganini, E. Giamello, O. Sacco, V. Vaiano and D. Sannino, *J. Energy Chem.*, 2017, **26**, 270–276.
- 48 A. Varkey and A. Fort, *Sol. Energy Mater. Sol. Cells*, 1993, **29**, 253–259.
- 49 B. Boruah, R. Gupta, J. M. Modak and G. Madras, *J. Photochem. Photobiol., A*, 2019, **373**, 105–115.
- 50 S. Sathasivam, B. A. Williamson, S. A. Althabaiti, A. Y. Obaid, S. N. Basahel, M. Mokhtar, D. O. Scanlon, C. J. Carmalt and I. P. Parkin, *ACS Appl. Mater. Interfaces*, 2017, **9**, 18031–18038.
- 51 T. El-Shazly, W. M. Hassan, S. T. A. Rahim and N. K. Allam, *Int. J. Hydrogen Energy*, 2015, **40**, 13867–13875.
- 52 Z. Weibin, W. Weidong, W. Xueming, C. Xinlu, Y. Dawei, S. Changle, P. Liping, W. Yuying and B. Li, *Surf. Interface Anal.*, 2013, **45**, 1206–1210.
- 53 B. Boruah, R. Gupta, J. M. Modak and G. Madras, *J. Photochem. Photobiol., A*, 2019, **373**, 105–115.
- 54 S. Farsinezhad, H. Sharma and K. Shankar, *Phys. Chem. Chem. Phys.*, 2015, **17**, 29723–29733.
- 55 Y. Abdollahi, A. Abdullah, Z. Zainal and N. Yusof, *Int. J. Basic Appl. Sci.*, 2011, **11**, 62–69.
- 56 N. Usha, R. Sivakumar, C. Sanjeeviraja and M. Arivanandhan, *Optik*, 2015, **126**, 1945–1950.
- 57 V. Agrahari, M. C. Mathpal, M. Kumar and A. Agarwal, *J. Alloys Compd.*, 2015, **622**, 48–53.
- 58 J. Liqiang, Q. Yichun, W. Baiqi, L. Shudan, J. Baojiang, Y. Libin, F. Wei, F. Honggang and S. Jiazhong, *Sol. Energy Mater. Sol. Cells*, 2006, **90**, 1773–1787.



- 59 S. P. Phivilay, A. A. Puretzky, K. Domen and I. E. Wachs, *ACS Catal.*, 2013, **3**, 2920–2929.
- 60 A. K. Simlandy, B. Bhattacharyya, A. Pandey and S. Mukherjee, *ACS Catal.*, 2018, **8**, 5206–5211.
- 61 N. Sobana, K. Selvam and M. Swaminathan, *Sep. Purif. Technol.*, 2008, **62**, 648–653.
- 62 S. Nethaji, A. Sivasamy, G. Thennarasu and S. Saravanan, *J. Hazard. Mater.*, 2010, **181**, 271–280.
- 63 R. J. Tayade, T. S. Natarajan and H. C. Bajaj, *Ind. Eng. Chem. Res.*, 2009, **48**, 10262–10267.
- 64 Y. Liu, Y. Ohko, R. Zhang, Y. Yang and Z. Zhang, *J. Hazard. Mater.*, 2010, **184**, 386–391.
- 65 A. Gürses, Ç. Doğan, M. Yalçın, M. Açıkyıldız, R. Bayrak and S. Karaca, *J. Hazard. Mater.*, 2006, **131**, 217–228.
- 66 L. Zhang, H. Li, Y. Liu, Z. Tian, B. Yang, Z. Sun and S. Yan, *RSC Adv.*, 2014, **4**, 48703–48711.
- 67 R. Godin, Y. Wang, M. A. Zwijnenburg, J. Tang and J. R. Durrant, *J. Am. Chem. Soc.*, 2017, **139**, 5216–5224.
- 68 M. Meetani, M. Rauf, S. Hisaindee, A. Khaleel, A. AlZamly and A. Ahmad, *RSC Adv.*, 2011, **1**, 490–497.
- 69 P. K. Samantaray, S. Baloda, G. Madras and S. Bose, *J. Mater. Chem. A*, 2018, **6**, 16664–16679.
- 70 F. Zhou and Y. Zhu, *J. Adv. Ceram.*, 2012, **1**, 72–78.
- 71 R. Gupta, N. K. Eswar, J. M. Modak and G. Madras, *Catal. Today*, 2018, **300**, 71–80.
- 72 R. Georgiev, B. Georgieva, M. Vasileva, P. Ivanov and T. Babeva, *Adv. Condens. Matter Phys.*, 2015, **2015**, 403196.
- 73 C.-H. Wu and J.-M. Chern, *Ind. Eng. Chem. Res.*, 2006, **45**, 6450–6457.

